JACS
JOURNAL OF THE AMERICAN CHEMICAL SOCIETY

ARTICLE

pubs.acs.org/JACS

Kirkendall Effect and Lattice Contraction in Nanocatalysts: A New Strategy to Enhance Sustainable Activity

Jia X. Wang,*[,†] Chao Ma,[‡,§] YongMan Choi,[†] Dong Su,[∥] Yimei Zhu,[‡] Ping Liu,[†] Rui Si,[†] Miomir B. Vukmirovic,[†] Yu Zhang,[†] and Radoslav R. Adzic*[,†]

[†]Chemistry Department, [‡]Condensed Matter Physics and Materials Science Department, [∥]Center for Functional Nanomaterials, Brookhaven National Laboratory, Upton, New York 11973, United States

[§]Beijing National Laboratory for Condensed Matter Physics, Institute of Physics, Chinese Academy of Sciences, Beijing 100190, China

Supporting Information

ABSTRACT: Core−shell nanoparticles increasingly are found to be effective in enhancing catalytic performance through the favorable influence of the core materials on the active components at the surface. Yet, sustaining high activities under operating conditions often has proven challenging. Here we explain how differences in the components' diffusivity affect the formation and stability of the core−shell and hollow nanostructures, which we ascribe to the Kirkendall effect. Using Ni nanoparticles as the templates, we fabricated compact and smooth Pt hollow nanocrystals that exhibit a sustained enhancement in Pt mass activity for oxygen reduction in acid fuel cells. This is achieved by the hollow-induced lattice contraction, high surface area per mass, and oxidation-resistant surface morphology—a new route for enhancing both the catalysts' activity and durability. The results indicate challenges and opportunities brought by the nanoscale Kirkendall effect for designing, at the atomic level, nanostructures with a wide range of novel properties.

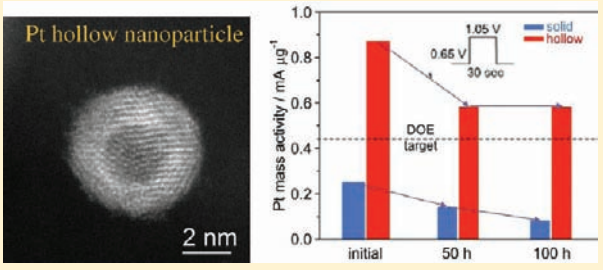

INTRODUCTION

The rapidly increasing demand for natural resources worldwide challenges scientists to develop renewable energy technologies with minimal use of scarce, expensive materials, such as platinum, the best single metal catalyst for the reactions in proton exchange membrane (PEM) fuel cells.[1,2] Enhanced Pt mass activities for the oxygen reduction reaction (ORR) in PEM fuel cells were obtained with core−shell nanocatalysts having an ultrathin Pt shell[3−6] on a core containing other metals. In addition to an increase in surface area per Pt mass, high enhancements in the area-normalized specific activity over Pt nanoparticles were found with Pt- or Pd-alloy cores containing 3d transition metals, such as Co, Ni, and Cu. However, a more challenging issue emerged as accelerated durability tests showed a gradual loss of surface area and ORR activity for these advanced ORR catalysts.[6−9] On the positive side, the Pt shells remained intact whether they were made by Pt monolayer deposition on a core nanoparticle[6,9] or via Pt enrichment at the surface by dissolving off the non-Pt components of an alloy nanoparticle.[7,8] The favorable or neutral segregation energy[10] ensures a high enrichment of Pt at the surface, and the increased dissolution potentials for Pt on more reactive metals than on itself[11] makes the thin Pt shells less prone to dissolution. However, the seemingly unstoppable loss of core materials is not well understood and raises the question of whether the enhancement in Pt mass activity is sustainable in acid fuel cells. Here, we first explain the persistent dissolution based on the nanoscale Kirkendall effect; thereafter, we demonstrate a new strategy to sustain activity enhancement by using hollow-induced lattice contraction on Pt shells.

The Kirkendall effect is a vacancy-mediated diffusion mechanism proposed on the basis of the observation of a net mass flow of a faster diffusing species balanced by the opposing flow of vacancies that condense into voids in solids.[12] Because of the enormously increased surface-area-to-volume ratio of nanomaterials, hollow nanoparticles[13−15] or nanoporous materials[16] may form by an outward flow of the faster diffusing species in responding to a reactive environment. The nanoscale Kirkendall effect also may engender undesirable consequences, for example, the instability of core−shell nanocatalysts, as mentioned above. In a mildly corrosive environment, the faster diffusing 3d transition metals flow out through lattice vacancies to the Pt surface, where they subsequently dissolve. Therefore, even though a pinhole-free Pt shell forms, the slow dissolution of activity-enhancing components in the core may persist. This understanding led us to a new strategy for designing active, durable ORR catalysts.

A hollow core is an interesting structure because it may induce a desirable lattice contraction in a Pt shell without engendering the instability caused by dissolution of core materials. Since the ORR rate at high potentials is limited by the steps involving the desorption of O and OH reaction intermediates,[17,18] weakening

Received: May 17, 2011
Published: July 24, 2011

ACS Publications © 2011 American Chemical Society

the strength of oxygen binding by lattice contraction[19,20] is an effective route to enhance the ORR activity on nanocatalysts.[4,21] Pt hollow nanoparticles made with Ag templates exhibit enhanced ORR activities but are not highly active and durable.[22,23] Likely, their instability is due to their porous[22] or dendrite-like[23] shells because low-coordination sites are prone to dissolution.[24,25] To achieve high, sustainable ORR activity, we developed methods to synthesize compact, smooth Pt hollow nanoparticles.

METHODS

Ni nanoparticles were electrodeposited on carbon powder support (~60 μg cm^{-2} Vulcan 72C, on a glassy carbon rotating electrode) by a single potential pulse, typically about 0.4 s at −1.4 V and 20 s at −0.8 V (vs Ag/AgCl, 3 M NaCl), in a deaerated solution of 0.1 M $NiSO_4$ and 0.5 M H_3BO_3. Within 10 min, the open-circuit potential rose to a stable value. Then the electrode was transferred into deaerated K_2PtCl_4 solution without exposure to air. Pt ions were reduced by metallic Ni with the amount controlled by the concentration of K_2PtCl_4 (0.05−1 mM) and the duration of galvanic replacement (3−30 min). After rotating the electrode in pure water to eliminate residual metal ions, about 20 potential cycles from 0.05 to 1.2 V versus the reversible hydrogen electrode (RHE) were carried out in a deaerated 0.1 M $HClO_4$ solution to completely dissolve Ni. The mass of metal components was determined using inductively coupled plasma mass spectrometry. For large-scale synthesis, Ni nanoparticles can be made using $NaBH_4$ as the reducing agent or other methods, and acid treatment is effective for removing the remaining Ni after partial galvanic replacement. Details will be published elsewhere after optimizing the synthesis procedures.

We measured the electrochemical surface area using the integrated hydrogen-desorption charges from the voltammetry curves, assuming 0.21 mC cm^{-2}. The ORR polarization curves were measured in forward potential sweep at 10 mV s^{-1} with a 1600 rpm rotation rate. The kinetic current at 0.9 V was calculated using $j_k = j/(1 - j/j_L)$, where j is the measured value at 0.9 V and j_L is the mass transport limiting current below 0.5 V. The solid Pt nanoparticle sample is commonly used Pt/C (45% Pt by weight on Vulcan 72 carbon powder).

High-resolution transmission electron microscopy (TEM) imaging and electron diffraction measurements were performed using the JEM-2200MCO transmission electron microscope equipped with two aberration correctors and an in-column Omega Filter. Electron diffraction was used to determine average lattice constants of the Pt hollow nanoparticles. All of the data were acquired under the same conditions as that for a standard gold-nanoparticle sample, and the positions of diffraction rings at intensity maxima were quantified to a single pixel. The uncertainty of the deduced lattice constant is about 0.001 nm determined by the deviation from the average of the values obtained from four low-index diffractions. Scanning TEM (STEM) measurements were performed using the Hitachi HD2700C equipped with a cold field emission electron source and a probe aberration corrector. In a vibration-isolated and temperature-stabilized room, the spatial resolution is superior to 0.1 nm.[26] The Z^x-contrast (Z is the atomic number and x = 1.4−2) STEM images were taken using a high-angle annular dark-field (HAADF) detector with 27 mrad convergence angle and collection angles between 114 and 608 mrad in this study. We heated the samples using a double-tile Gatan heating holder under a vacuum of ~10^{-6} Pa.

X-ray diffraction experiments were carried out on beamline X7B (λ = 0.3184 Å) of the National Synchrotron Light Source at Brookhaven National Laboratory. Sample powders were loaded into a 0.5 mm glass capillary. Two-dimensional powder patterns were collected with a Perkin Elmer image plate detector, and the diffraction rings were integrated using the FIT2D code.[27] The fitted parameters (lattice constant, particle size, and microstrain) were obtained through a Rietveld refinement.[28−30] Lanthanum hexaboride (LaB_6) was used as the instrumental reference.

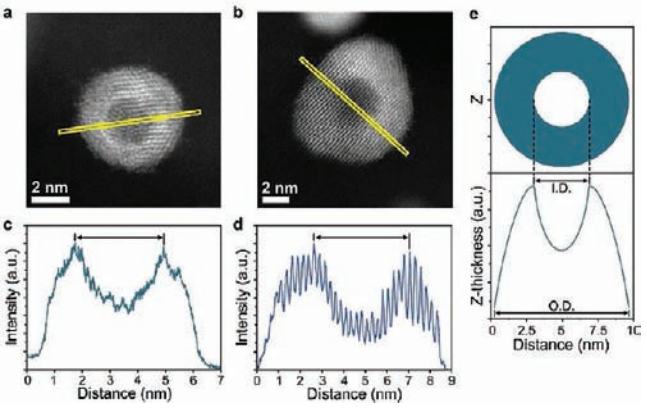

Figure 1. (a, b) High-resolution STEM images of Pt hollow particles. (c, d) Line-scans of the intensity profile nearly parallel (c) and perpendicular (d) to the direction of the lattice plane. (e) Calculated z-thickness versus x-distance at the y = 0 position for a hollow sphere.

Density functional theory calculations were performed using the Vienna ab initio simulation package (VASP)[31,32] with the projector augmented wave method (PAW).[33] The generalized gradient approximation (GGA) using the revised Perdew−Burke−Ernzerholf (RPBE) functional[34] was utilized to describe the exchange and correlation energies. We constructed a spherelike nanoparticle model as shown in Figure 5c and fully optimized the structures. Only the Γ point was used for **k** sampling, which is an effective approach for nonperiodic systems,[35] and the cutoff energy was 400 eV. In our calculations, the 1.7 nm clusters were used to model the solid and hollow nanoparticles. Larger lattice contraction and consequently more weakened oxygen binding on the hollow particle support the experimentally found trend. Accurate modeling of larger nanoparticles is not currently practical for DFT due to high computational cost. The adsorption of atomic O at the (111) terrace of a nanoparticle was calculated as a descriptor for scaling ORR activity. The binding energy of oxygen (BE-O) is defined as BE-O = E[O−NP] − E[NP] − E[O], where E[O−NP], E[NP], and E[O] are the calculated electronic energies of an adsorbed oxygen species on a nanoparticle, a clean nanoparticle, and triplet oxygen atom. Then, the differences of BE-O of NPs (ΔBE-O) were calculated relative to the BE-O on Pt(111) (−4.09 eV).

RESULTS AND DISCUSSION

Ni nanoparticles were found suitable as templates to facilitate the formation of single-void particles with complete Pt shells. Compared to commonly used Ag templates[15] or other relatively noble metals, such as Cu, Ni has considerably lower reduction potential and can be more easily dissolved in acid solution. These properties appear to be responsible for the formation of nonporous, pure Pt hollow particles unreported previously. In one method, we first electrodeposited Ni nanoparticles on carbon powder supports, followed by their partial galvanic replacement to form Ni−Pt core−shell nanoparticles. The remaining Ni readily dissolved away within 20 potential cycles in acid solutions, resulting in Pt hollow nanospheres. We confirmed the complete removal of Ni using electron energy loss spectroscopy in TEM measurements and by mass determination using inductively coupled plasma mass spectrometry (ICP-MS). We also synthesized Ni nanoparticles using $NaBH_4$. Acid wash (pH 1 H_2SO_4 or $HClO_4$) was used to remove the remaining Ni after galvanic replacement reaction with Pt ions. The Ni content in the catalyst was found by ICP-MS to be less than 0.5% by weight.

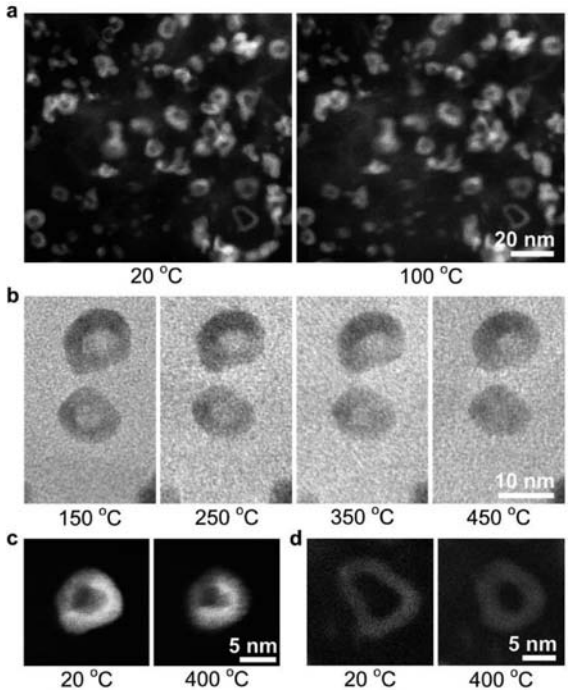

Figure 2. (a) STEM images of Pt hollow nanoparticles measured at 20 and 100 °C (after 1 h). (b) TEM images taken at several temperatures during stepwise heating up at a rate of 50 °C/half-hour. (c, d) STEM images measured at 20 °C before and after 1 h annealing at 400 °C.

We identified compact Pt hollow nanoparticles in high-resolution STEM images for the samples after electrochemical measurements and tests of the catalyst's durability. Particles with a single lattice orientation across the entire particle, as depicted in Figure 1a,b, denote the formation of hollows via lattice vacancy exchange; i.e., channels or pinholes are not necessary to remove the Ni cores. The sizes of the hollows are determined from the distances between the intensity maxima along the line scans shown in Figure 1c,d because, as illustrated in Figure 1e, the maxima in the vertical thicknesses occur at the edges of a hollow. We varied synthetic parameters to optimize the ORR activity and durability. The best catalytic activity was found with the 3−9 nm hollow spheres with a 1−2 nm thick shell, equivalent to 4−8 atomic layers.

Since a PEM fuel cell operates at 80 °C, we checked the thermal stability of the Pt hollow nanoparticles using in situ TEM to monitor the structure changes at elevated temperatures. The samples were heated under vacuum. STEM images in Figure 2a show no changes after an hour at 100 °C. The hollow particles started to shrink above 250 °C as the temperature was raised in steps at 50 °C/half-hour, as depicted in the TEM images measured at several holding temperatures (Figure 2b). The STEM images taken at 20 °C after 1 h annealing at 400 °C (Figure 2c,d) showed moderate shrinking of the hollow, but not its elimination. These observations indicate their much higher thermal stability than that estimated for gold hollow particles.[36] The main reason likely is the lower diffusivity of Pt than Au.[37] Generally, metals with higher melting temperatures have lower diffusivities and thus better stability. Particles also became more rounded as annealing often yields structures with lower surface energy.

We compared the ORR activity of Pt hollow nanoparticles with that of Pt solid nanoparticles using the rotating disk electrode method at room temperature. While similar kinetic currents at 0.9 V were obtained from the two ORR polarization curves (Figure 3a), their voltammetry curves in the inset differ significantly due to mainly a 4-fold difference in the samples' Pt mass loadings. Electrochemical surface areas (ESAs) were determined by integrated hydrogen desorption charges, which were used to calculate the ESA per Pt mass and ORR specific activity shown in Figure 3b. The surface area per mass is similar for the two samples with the average particle size larger for hollow (6.5 nm) than for solid (3.2 nm) particles. That means the effect of significant mass-saving by hollow core in the former is about the same as that of increased ratio of surface atoms on smaller particles in the latter. Thus, the 4.4-fold enhancement in Pt mass activity, which equals the product of ESA per Pt mass and ESA-normalized specific activity, mainly results from increased specific activity.

More importantly, the enhanced Pt mass activity on Pt hollow nanospheres is highly sustainable in potential cycling tests. We first found that 10 000 potential cycles, swept between 0.65 and 1.05 V at 50 mV s^{-1}, did not cause any loss in ESA and ORR activities. We then used pulsed potential cycles, 30 s alternatively at 0.65 and 1.05 V. Stepping between two limiting potentials with a long dwell time is a more severe test than linear sweeping cycles because the dissolution of the low-coordinate atoms is most rapid at 0.65 V, and the regeneration of defects, apparent by surface roughening, is most pronounced at the high potential limit. This mechanism is supported by the high dissolution rate at steps on Pt(111) at 0.65 V and the 0.6 nm deep holes observed over the entire surface area at 1.15 V.[38] As shown in Figure 4, there is about 33% loss in the ORR activity after 3000 pulse potential cycles in 50 h but no further loss thereafter. In another test, we found no loss of stabilized activity between 3000 and 10 000 pulse potential cycles lasting 7 days. In comparison, the ORR activity of solid Pt nanoparticles (3.2 nm average diameter, 45% Pt/C by weight), fell after 3000 cycles, and continued to do so during an additional 3000 of them. Figure 4b shows that the sustainable Pt mass activity on Pt hollow spheres is 0.58 mA μg^{-1}, 6-fold that on solid Pt nanoparticles after the 6000 cycle, 100 h durability tests. These results are significant because Pt-alloy catalysts maintained only about 2-fold enhancement in Pt mass activity compared to Pt nanoparticles after 5000 potential cycles (0.5−1.0 V at 100 mV s^{-1}) in PEM fuel cell tests.[7] The durability of the Pt-monolayer catalysts on Pd and Pd-alloy cores has been improving, but they still show a considerable loss of Pd under potential cycles above 1 V. This is largely due to the lower dissolution potential of Pd than that of Pt.

We attribute the remarkable sustainable ORR activity on Pt hollow nanospheres partly to the lattice contraction induced by the hollows. Figure 5a shows an example of well-calibrated electron diffraction measurements. An average lattice constant of 3.85 Å was determined from the positions of diffraction rings at intensity maxima for the imaged Pt hollow particles. The average lattice strain, ε_l, calculated by $(a - a_0)/a_0$ with a_0 = 3.923 Å for bulk Pt is −1.9%. Samples made with different synthesis parameters have shown lattice contraction ranging from −1.2 to −2.0%. To further confirm significant hollow-induced lattice contraction, we carried out X-ray diffraction measurements on Pt hollow nanoparticles synthesized from chemically reduced Ni nanoparticles. The average particle size was found smaller than those in the samples used in TEM measurements. From the peak positions, we deduced an average strain of −1.4% for Pt hollow particles, compared with 0.4% for solid Pt nanoparticles

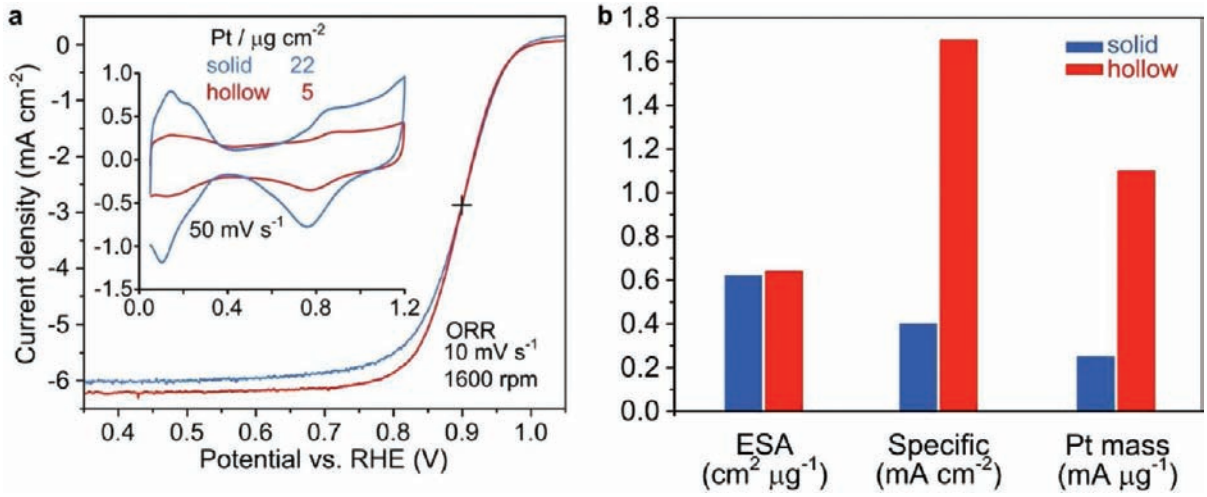

Figure 3. (a) ORR polarization and voltammetry (inset) curves in oxygen-saturated and deaerated 0.1 M $HClO_4$ solutions, respectively, for solid (blue) and hollow (red) Pt nanoparticle samples with 22 and 5 $\mu g\ cm^{-2}$ Pt loading, respectively. (b) Comparison of the ESA per Pt mass measured by hydrogen desorption charges and the ORR specific and Pt mass activities measured at 0.9 V in 10 mV s^{-1} potential sweeps.

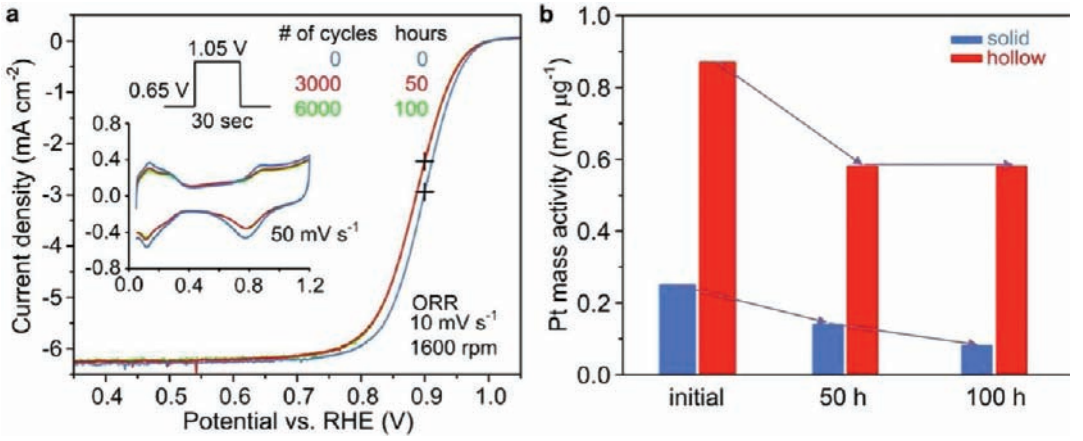

Figure 4. (a) Sequential ORR polarization and voltammetry (inset) curves for Pt hollow nanocatalysts. (b) Pt mass activity as a function of potential cycling time for Pt hollow and solid nanoparticles.

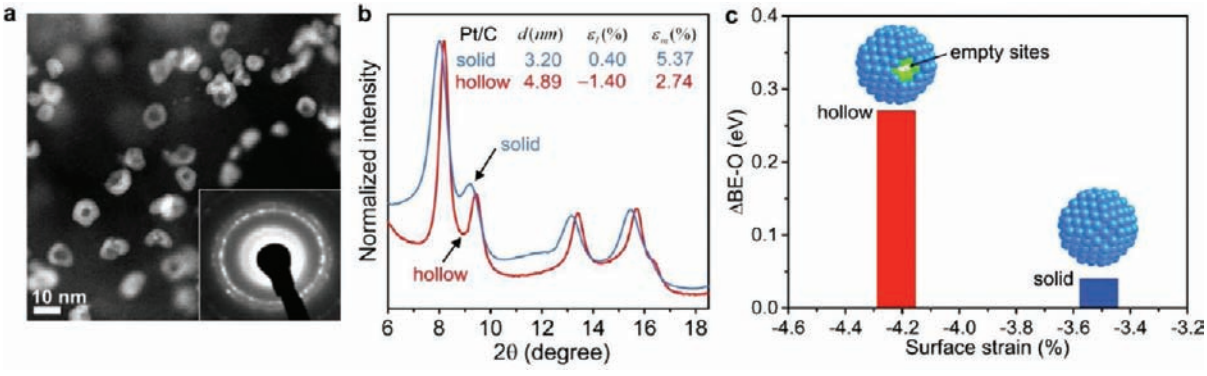

Figure 5. (a) Electron diffraction pattern (right-bottom corner) measured for Pt hollow nanoparticles. (b) Profiles of X-ray powder diffraction intensity for solid (blue) and hollow (red) Pt nanoparticles with obtained average particle diameter, d, average lattice strain, ε_l, and microstrain strain, ε_m, from fitting (see Methods and Figure S1 of the Supporting Information). (c) DFT calculated changes in binding energy of oxygen on Pt nanoparticles from that on Pt(111), −4.09 eV, versus calculated surface strains (average in-plane Pt−Pt distance of all surface atoms compared to that of DFT calculated bulk Pt, 2.824 Å) using solid and hollow (green color is used for the inner layer to clarify the bilayer-thick shell) spherelike models.

dx.doi.org/10.1021/ja204518x |J. Am. Chem. Soc. 2011, 133, 13551–13557

(Figure 5b). These results confirmed significant hollow-induced lattice contraction in the multilayer Pt shells.

To better understand the nanoscale effects on lattice spacing of metal nanoparticles, we note two recent findings: (1) The small particles, especially those below 5 nm, induce lattice contraction in metal nanoparticles due to the significant curvature effect,[21,25] experimentally demonstrated on Au, the noblest of metals,[39] and on Pt and Cu nanoparticles made and kept under vacuum;[40] and (2) a 5 nm air-exposed Pt nanoparticle exhibited a slightly expanded core, but up to 4.8% lattice expansion at the surface.[41] These observations suggest that, generally, lattice contraction on small metal nanoparticles is unobservable because the surface of most of them become oxidized in air at room temperature, including Pt (the second most noble metal); such surface oxidation causes lattice expansion affecting the entire particle. This effect is significant because it is amplified in a continuous cycle. Surface oxidation induces lattice expansion and roughens the nanoparticles' surface; such more loosely bounded surfaces are more prone to oxidation. Therefore, having a smooth, oxidation-resistant surface is important for sustaining lattice contraction in metal nanoparticles. While the air-formed surface oxide on Pt nanocatalysts is stable under vacuum, it can be easily removed electrochemically. Usually, its reduction current peak only appears in the first negative potential sweep from the open circuit potential.

By fitting the XRD intensity profiles,[42] we determined the lattice strain, ε_l, from the peaks' positions and the microstrain, ε_m, from the peaks' width and shape (see Figure S1 of the Supporting Information). The latter comes from locally generated stress caused by the presence of dislocations and point defects, resulting in nonuniform deviations in atomic distances from an average value, i.e., $\varepsilon_m = |a_d - a|/a$, that broaden the diffraction peaks, in addition to broadening due to particle size.[43−45] For metal nanoparticles, such microstrains often exhibit high values on surfaces rich in low-coordination sites, and that is associated with the lattice expansion due to oxygen adsorption on these sites. Under this condition, we can estimate the average atomic spacing using $a_s = a\,(1 + \varepsilon_m)$. Thus, the surface strain, defined as the average spacing of surface atoms with respect to that in the bulk Pt, is calculated by $\varepsilon_s = a_s/a_0 - 1 = (1 + \varepsilon_l)(1 + \varepsilon_m) - 1$. On the basis of the lattice strains and microstrains given in Figure 5b, the surface strains are 5.8 and 0.7%, respectively, for the solid- and hollow-particle samples. Our 5.8% surface strain for the Pt solid nanoparticles is consistent with up to 4.8% expansion at the surface of a Pt nanoparticle reported by a STEM study.[41] The hollow-particle sample has 50% smaller microstrain, suggesting there are fewer defects or low-coordination sites at the surface, consistent with our TEM observations of well-rounded hollow particles. The positive surface strains on solid and hollow particles indicate that the surface-oxidation-induced expansions overwhelm the nanoscale-induced contractions on small Pt nanoparticles. A change from positive to negative surface strain, i.e., having a net contraction on average with respect to the Pt(111) surface, can happen by improving the synthesis method to obtain a higher yield of well-rounded, compact hollow spheres.

We further verified the occurrence of hollow-induced lattice contraction from a theoretical point of view using DFT calculations. Since the structural optimization of sizable clusters is computationally intensive, we used the 1.7 nm solid and hollow (two atomic layer thick shell) spherelike models as shown in Figure 5c. The effects of a hollow on surface strain and oxygen binding energy are illustrated by comparing the calculated results

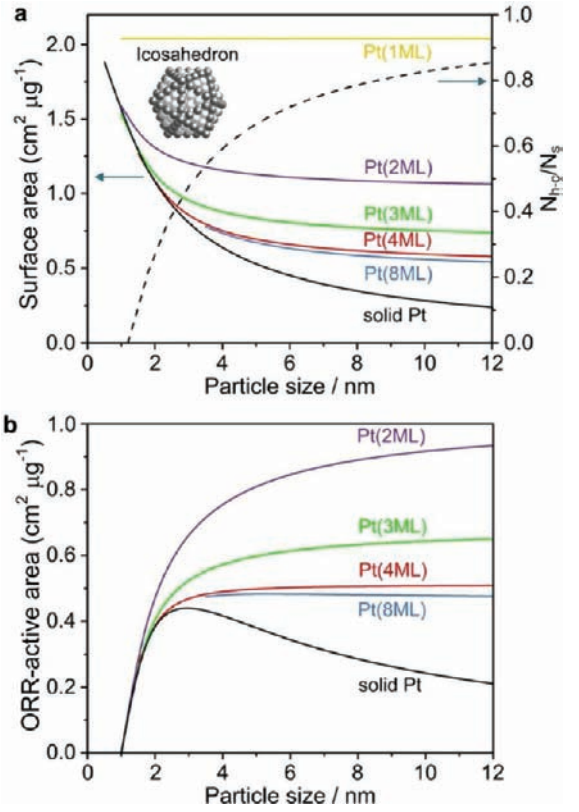

Figure 6. (a) Surface area per Pt mass and the ratio of high-coordination atoms to the total number of surface atoms, N_{h-c}/N_s, as a function of particle size calculated using an icosahedra cluster model. (b) ORR active area per Pt mass calculated by multiplying total surface area with N_{h-c}/N_s.

without experimental complications. The calculated surface strains display a larger lattice contraction on the hollow particle (−4.47%) than on the solid one (−3.26%), consistent with our experimental findings of a smaller atomic spacing for hollow samples (0.7%) than for solid (5.8%) ones despite the different signs in the surface strains. As discussed above, surface oxidation causes the lattice expansion of Pt nanoparticles, an effect that is not included in theoretical modeling. In addition, we expect a smaller surface contraction for larger nanoparticles with and without hollow since their curvature flattens out with increasing particle size. Thus, the size gap (1.7 nm model versus >3 nm particles in the samples) also restricts a direct comparison. Nevertheless, the DFT calculations verified higher lattice contraction and weaker oxygen binding (Figure 5c) on hollow than solid Pt nanoparticles. Previously reported enhancements in ORR specific activity result from the weakened oxygen binding energy through mismatch-induced lattice contraction and/or the ligand effect, as demonstrated with Pt_3Ni single crystals[46] and Pt_3Y polycrystalline crystals.[47] Due to the instability of the non-noble metal in subsurface layers of nanoparticles under PEM fuel cell operating conditions, these effects may diminish when the Pt shell thickens. Thus, hollow-induced lattice contraction is a new route for sustaining enhanced ORR activity on nanocatalysts.

In addition to these effects of lattice contraction and smooth surface morphology, the favorable geometric effects of hollow particles also play an important role in enhancing mass activity and stability. Using a spherelike icosahedron cluster model, we

calculated the surface area per Pt mass as a function of particle size for solid and hollow Pt particles (see Supporting Information for more details on the formula used). As Figure 6a shows, the surface area per Pt mass is 2.04 cm^2 μg^{-1} for a monolayer-thick hollow particle, assuming the atomic density of that of the Pt(111) surface. For hollow particles with thicker shells, the surface area per mass decreases with increasing particle size. The value for a 4−8 monolayer-thick, 10 nm hollow particle is still about double that of the same-sized solid particle. Furthermore, we show (dashed line in Figure 6a) that for small nanoparticles, there is a sharp increase in the ratio of the high-coordinate sites on terraces to the total number of surface atoms, N_{h-c}/N_s, with increasing particle size. Because the ORR rate is limited by O- and OH-desorption on Pt[18] at high potentials, the less reactive high-coordinate (111) terraces are the most conducive to the ORR.[21,48] Thus, the product of surface area and N_{h-c}/N_s represents the ORR-active area (Figure 6b). The value for solid particle is at its maximum around 3 nm and declines with rising particle size. However, the rate of Pt dissolution increases sharply with declining size, especially below 5 nm.[24] The dilemma in optimizing particle size for high activity and durability is largely avoided with hollow particles, for which the ORR-active area per Pt mass is high from 3 to 12 nm.

In summary, we demonstrated, using atomically resolved STEM images, the formation of compact, nonporous Pt hollow nanospheres through partial galvanic replacement of Ni nanoparticles. This finding offers an opportunity to simultaneously enhance catalysts' activity and durability for the ORR. Favorable lattice contraction is achieved on compact Pt hollow nanoparticles without the complications stemmed from a less noble metal core. Although the inner surface of a complete hollow particle is not involved in reaction, a hollow nanoparticle affords larger particle size than a solid one with the same mass, thus significantly increasing the amount of the high-coordination surface sites per Pt mass. Such sites are very important for enhancing the ORR activity and catalyst's stability. Besides electrodeposition, which is convenient for tuning the size of Ni particles, we synthesized Pt-hollow catalysts using wet chemical synthesis method and used these particles in XRD studies. We found that the surface strain of metal nanoparticles, determined by XRD-measured lattice strain and microstrain, strongly correlates with the ORR catalysts' performance. Hence it affords us a useful tool in further optimizing synthesis conditions. Without size- and/or shape-control agents, the synthesis methods developed are environmentally friendly and low cost, illustrating the promise of nanoengineering for practical applications.

■ ASSOCIATED CONTENT

Ⓢ Supporting Information. Figures showing profiles of Rietveld refinement results on Pt solid (a) and hollow (b) nanocrystals and text describing the formula for calculating surface area per Pt mass. This material is available free of charge via the Internet at http://pubs.acs.org.

■ AUTHOR INFORMATION

Corresponding Author

*Tel.: +1-631-344-4522 (R.R.A.); +1-631-344-2515 (J.X.W.). E-mail: adzic@bnl.gov (R.R.A); jia@bnl.gov. (J.X.W.). Fax: +1-631-344-5815 (J.X.W.).

■ ACKNOWLEDGMENT

This work is supported by U.S. Department of Energy, Basic Energy Sciences, Divisions of Chemical and Material Sciences, Material Sciences and Engineering Division, under the Contract No. DE-AC02-98CH10886. DFT calculations were performed at the Center for Functional Nanomaterials, Brookhaven National Laboratory and the National Energy Research Scientific Computing (NERSC) Center. We thank Prof. M. C. Lin for CPU time and Jonathan Hanson and Hugh Isaacs for discussions.

■ REFERENCES

(1) Service, R. F. *Science* **2009**, *324*, 1257.
(2) Gasteiger, H. A.; Kocha, S. S.; Sompalli, B.; Wagner, F. T. *Appl. Catal., B* **2005**, *56*, 9.
(3) Srivastava, R.; Mani, P.; Hahn, N.; Strasser, P. *Angew. Chem., Int. Ed.* **2007**, *46*, 8988.
(4) Strasser, P.; Koh, S.; Anniyev, T.; Greeley, J.; More, K.; Yu, C. F.; Liu, Z. C.; Kaya, S.; Nordlund, D.; Ogasawara, H.; Toney, M. F.; Nilsson, A. *Nat. Chem.* **2010**, *2*, 454.
(5) Adzic, R. R.; Zhang, J.; Sasaki, K.; Vukmirovic, M. B.; Shao, M.; Wang, J. X.; Nilekar, A. U.; Mavrikakis, M.; Valerio, J. A.; Uribe, F. *Top. Catal.* **2007**, *46*, 249.
(6) Shao, M. H.; Shoemaker, K.; Peles, A.; Kaneko, K.; Protsailo, L. *J. Am. Chem. Soc.* **2010**, *132*, 9253.
(7) Neyerlin, K. C.; Srivastava, R.; Yu, C. F.; Strasser, P. *J. Power Sources* **2009**, *186*, 261.
(8) Chen, S.; Gasteiger, H. A.; Hayakawa, K.; Tada, T.; Shao-Horn, Y. *J. Electrochem. Soc.* **2010**, *157*, A82.
(9) Zhou, W. P.; Sasaki, K.; Su, D.; Zhu, Y. M.; Wang, J. X.; Adzic, R. R. *J. Phys. Chem. C* **2010**, *114*, 8950.
(10) Ruban, A. V.; Skriver, H. L.; Norskov, J. K. *Phys. Rev. B* **1999**, *59*, 15990.
(11) Greeley, J.; Norskov, J. K. *Electrochim. Acta* **2007**, *52*, 5829.
(12) Smigelakas, A. D.; Kirkendall, E. O. *AIME* **1947**, *171*, 130.
(13) Yin, Y. D.; Rioux, R. M.; Erdonmez, C. K.; Hughes, S.; Somorjai, G. A.; Alivisatos, A. P. *Science* **2004**, *304*, 711.
(14) Fan, H. J.; Gosele, U.; Zacharias, M. *Small* **2007**, *3*, 1660.
(15) Chen, H. M.; Liu, R. S. *J. Phys. Chem. C* **2011**, *115*, 3513.
(16) Hu, Y. S.; Guo, Y. G.; Sigle, W.; Hore, S.; Balaya, P.; Maier, J. *Nat. Mater.* **2006**, *5*, 713.
(17) Wang, J. X.; Markovic, N. M.; Adzic, R. R. *J. Phys. Chem. B* **2004**, *108*, 4127.
(18) Wang, J. X.; Zhang, J. L.; Adzic, R. R. *J. Phys. Chem. A* **2007**, *111*, 12702.
(19) Norskov, J. K.; Rossmeisl, J.; Logadottir, A.; Lindqvist, L.; Kitchin, J. R.; Bligaard, T.; Jonsson, H. *J. Phys. Chem. B* **2004**, *108*, 17886.
(20) Kitchin, J. R.; Norskov, J. K.; Barteau, M. A.; Chen, J. G. *Phys. Rev. Lett.* **2004**, *93*, 156801.
(21) Wang, J. X.; Inada, H.; Wu, L. J.; Zhu, Y. M.; Choi, Y. M.; Liu, P.; Zhou, W. P.; Adzic, R. R. *J. Am. Chem. Soc.* **2009**, *131*, 17298.
(22) Chen, H. M.; Liu, R. S.; Lo, M. Y.; Chang, S. C.; Tsai, L. D.; Peng, Y. M.; Lee, J. F. *J. Phys. Chem. C* **2008**, *112*, 7522.
(23) Peng, Z. M.; Wu, J. B.; Yang, H. *Chem. Mater.* **2010**, *22*, 1098.
(24) Rinaldo, S. G.; Stumper, J.; Eikerling, M. *J. Phys. Chem. C* **2010**, *114*, 5773.
(25) Wang, L. Y.; Roudgar, A.; Eikerling, M. *J. Phys. Chem. C* **2009**, *113*, 17989.
(26) Inada, H.; Wu, L. J.; Wall, J.; Su, D.; Zhu, Y. M. *J. Electron Microsc.* **2009**, *58*, 111.
(27) Hammersley, A. P.; Svensson, S. O.; Thompson, A. *Nuclear Instruments and Methods in Physics Research Section A: Accelerators, Spectrometers, Detectors and Associated Equipment*; Elsevier: Amsterdam, 1994; Vol. 346, p 312.
(28) Larson, A. C.; von Dreele, R. B. *GSAS General Structure Analysis System*, Los Alamos National Laboratory: Los Alamos, NM, 1995.
(29) Rietveld, H. M. *J. Appl. Crystallogr.* **1969**, *2*, 65.

(30) Toby, B. H. *J. Appl. Crystallogr.* **2001**, *34*, 210.
(31) Kresse, G.; Hafner, J. *Phys. Rev. B* **1993**, *47*, 558.
(32) Kresse, G.; Furthmuller, J. *Phys. Rev. B* **1996**, *54*, 11169.
(33) Blochl, P. E. *Phys. Rev. B* **1994**, *50*, 17953.
(34) Hammer, B.; Hansen, L. B.; Norskov, J. K. *Phys. Rev. B* **1999**, *59*, 7413.
(35) Loschen, C.; Migani, A.; Bromley, S. T.; Illas, F.; Neyman, K. M. *Phys. Chem. Chem. Phys.* **2008**, *10*, 5730.
(36) Tu, K. N.; Gosele, U. *Appl. Phys. Lett.* **2005**, *86*, 093111.
(37) Seebauer, E. G.; Allen, C. E. *Prog. Surf. Sci.* **1995**, *49*, 265.
(38) Komanicky, V.; Chang, K. C.; Menzel, A.; Markovic, N. M.; You, H.; Wang, X.; Myers, D. *J. Electrochem. Soc.* **2006**, *153*, B446.
(39) Huang, W. J.; Sun, R.; Tao, J.; Menard, L. D.; Nuzzo, R. G.; Zuo, J. M. *Nat. Mater.* **2008**, *7*, 308.
(40) Wasserma, Hj; Vermaak, J. S. *Surf. Sci.* **1972**, *32*, 168.
(41) Du, K.; Emst, F.; Pelsozy, M. C.; Barthel, J.; Tillmann, K. *Acta Mater.* **2010**, *58*, 836.
(42) Dekeijser, T. H.; Langford, J. I.; Mittemeijer, E. J.; Vogels, A. B. P. *J. Appl. Crystallogr.* **1982**, *15*, 308.
(43) Axelsson, A. K.; Aguesse, F.; Spillane, L.; Valant, M.; McComb, D. W.; Alford, N. M. *Acta Mater.* **2011**, *59*, 514.
(44) Si, R.; Zhang, Y. W.; Li, S. J.; Lin, B. X.; Yan, C. H. *J. Phys. Chem. B* **2004**, *108*, 12481.
(45) Kurakevych, O. O.; Chauveau, T.; Solozhenko, V. L. *J. Superhard Mater.* **2010**, *32*, 231.
(46) Stamenkovic, V. R.; Fowler, B.; Mun, B. S.; Wang, G. F.; Ross, P. N.; Lucas, C. A.; Markovic, N. M. *Science* **2007**, *315*, 493.
(47) Greeley, J.; Stephens, I. E. L.; Bondarenko, A. S.; Johansson, T. P.; Hansen, H. A.; Jaramillo, T. F.; Rossmeisl, J.; Chorkendorff, I.; Norskov, J. K. *Nat. Chem.* **2009**, *1*, 552.
(48) Zhang, J.; Yang, H.; Fang, J.; Zou, S. *Nano Lett.* **2010**, *10*, 638.